

Empirical mode decomposition profilometry: small-scale capabilities and comparison to Fourier transform profilometry

GUILLAUME LAGUBEAU,^{1,2,*} PABLO COBELLI,^{1,3} TOMASZ BOBINSKI,¹ AGNÈS MAUREL,⁴ VINCENT PAGNEUX,⁵ AND PHILIPPE PETITJEANS¹

¹Physique et Mécanique des Milieux Hétérogènes PMMH, UMR CNRS 7636-ESPCI-UMPC Univ. Paris 6–UPD Univ., Paris 7, France

²Departamento de Física, Universidad de Santiago de Chile, Santiago, Chile

³Departamento de Física, Facultad de Ciencias Exactas y Naturales, Universidad de Buenos Aires and IFIBA, CONICET, Ciudad Universitaria, 1428 Buenos Aires, Argentina

⁴Institut Langevin, UMR 7587, 1 rue Jussieu 75005 Paris, France

⁵Laboratoire d'Acoustique de l'Université du Maine, UMR CNRS 6613, Avenue Olivier Messiaen, 72085 Le Mans, France

*Corresponding author: guillaume.lagubeau@usach.cl

Received 6 August 2015; revised 16 September 2015; accepted 16 September 2015; posted 17 September 2015 (Doc. ID 247491); published 3 November 2015

We present the empirical mode decomposition profilometry (EMDP) for the analysis of fringe projection profilometry (FPP) images. It is based on an iterative filter, using empirical mode decomposition, which is free of spatial filtering and adapted for surfaces characterized by a broadband spectrum of deformation. Its performances are compared to Fourier transform profilometry, the benchmark of FPP. We show both numerically and experimentally that using EMDP improves strongly the profilometry small-scale capabilities. Moreover, the height reconstruction distortion is much lower: the reconstructed height field is now both spectrally and statistically accurate. EMDP is thus particularly suited to quantitative experiments. © 2015 Optical Society of America

OCIS codes: (120.0120) Instrumentation, measurement, and metrology; (100.2650) Fringe analysis; (100.5070) Phase retrieval.

<http://dx.doi.org/10.1364/AO.54.009409>

1. INTRODUCTION

Fringe projection profilometry (FPP) is an instrument of choice for the measurement of fast dynamic events [1]: it avoids the use of moving parts and, with an adapted algorithm, needs no more than one image to recover the height field. Recently, it has been greatly developed and enhanced. In particular, an adaptation of this technique opened a new experimental field by allowing the instantaneous measurement of the full height map of a free surface [2].

The standard FPP setting is the following: a sinusoidal fringe pattern of wavenumber k_0 is projected onto the surface under study. The projection is observed and registered from a different viewpoint by a camera (different geometrical configurations are possible as summarized in [3]). In the viewpoint of the camera, a surface deformation corresponds to a distortion, i.e., the local phase changes, of the fringe pattern. The challenge created by the use of a single image is that it contains only an intensity field $I(x, y)$ from which a phase retrieval has to be achieved. Following Takeda's formulation [4,5], the light intensity registered by the camera can be described as

$$I(x, y) = A(x, y) \cos[k_0 x + \phi(x, y)] + B(x, y), \quad (1)$$

the local mean $B(x, y)$ and amplitude $A(x, y)$ of the fringe pattern have to be estimated for recovering the phase $\phi(x, y)$. Using a frequency space algorithm such as Fourier transform profilometry (FTP), this step acts as a low-pass filter for the height reconstruction as we show later in this paper.

Due to its practical applications and its single-shot capabilities, FTP has had a great success. However, its intrinsic properties naturally imply a major limitation. As the filtering is performed in the Fourier space, the width of the filtering window determines the spectral content that is recovered from a measurement. Namely, the fundamental spectrum must be separated from zeroth- and higher-order spectra [6,7]. A lot of effort has been put into enhancing and improving the technique in the sense of overcoming these limitations (the reader is referred to the exhaustive reviews by [8,9] and references therein). However, the issue of narrow-bandedness still remains as it originates from the bandpass filtering process which is inherent to the technique. A different approach for single-shot FPP is needed in the case of spatially broadband signals. Huang and co-workers [10,11] introduced a filtering method called empirical mode decomposition (EMD), which was further explored by Flandrin *et al.* [12,13], for decomposing a nonstationary and nonlinear

signal into amplitude and frequency modulations. Due to its properties, it is well suited for separating the amplitude modulation from the carrier component in fringe profilometric images. The possibility of implementing such a decomposition has been studied before and strategies have been proposed [14–18], however, none of these are designed for broadband signals.

In this paper we propose a novel fringe processing technique based on the EMD principle that allows for the separation of the envelope, the mean value, and the carrier preserving the broadband information on the original signal. Determining local maxima and minima presents inherent difficulties (namely, mode mixing). The algorithm proposed in the present work solves this problem for profilometric purposes.

The paper is organized as follows. In the first part, the EMDP is presented. In the following sections, two examples of reconstruction by EMDP for both synthetic and experimental 2D signals illustrate its performances that are compared to FTP, being the benchmark of FPP.

2. EMDP ALGORITHM

The EMD decomposes a signal into a sum of modes called intrinsic mode functions (IMFs) and a residual, using an iterative algorithm [10]. Each IMF is an alternating signal of zero local mean, with all its maxima positive and all its minima negative, and is thus well-suited for local phase measurement.

Note that if A and B in Eq. (1) are not space dependent, the signal is perfectly equivalent to an IMF. Consequently, performing the EMD decomposition on that hypothetical signal would result in the first IMF containing only the modulated carrier signal and a residual being the constant B , making phase extraction a straightforward process. However, realistic fringe profilometric images are characterized by contrast and the mean illumination which depend on space, as well as by the presence of noise. With such a signal, the EMD decomposition spreads the modulated carrier over several IMFs, a phenomenon called “mode mixing” [10,11,19,20] in which an IMF contains local oscillations with disparate frequencies or scales. In order to recover the carrier, one approach is to sum the IMFs on which it is spread [14]. However, this raises two difficulties. First, the determination of the relevant IMFs is ambiguous. Second, a sum of IMFs is *a priori* not an IMF, and thus it forces one to use the FTP algorithm before recovering the phase [14].

We present here an algorithm that resolves these issues by recovering the carrier unambiguously and without resorting to the Fourier transform. As this novel fringe processing technique replaces the Fourier transform filtering in FTP by a decomposition in direct space based upon the EMD algorithm, we named it empirical mode decomposition profilometry (EMDP). The EMDP technique effectively filters the signal so that the first intrinsic mode function provided by the EMD contains the carrier. In other words, the first IMF has to be that of largest amplitude at each point. For this, we take advantage of the EMD which allows one to locally filter the amplitudes independently of the frequencies.

Our algorithm is based on the comparison of the amplitudes of the first IMF with the others upon disjoint segments separated by the first IMF's zero-crossings. Wherever the first IMF is not the one of maximal amplitude, the corresponding segment is

filtered out from the first IMF. It is worth noting that such segment filtering is the most local (pointwise) filtering operation that can be performed on the IMFs without altering the continuity of the signal. Then, the signal is recomposed by summing the filtered first IMF with the others (as well as the residual) and the process is iterated until the first IMF is the one with the largest amplitude at each point. Once obtained, the envelope of the resulting IMF is normalized according to [21] and the phase extraction process is performed by direct quadrature [21].

More explicitly, given a signal $s(x)$ the operations involved in the proposed EMDP algorithm can be summarized as follows:

1. Perform the EMD decomposition of the signal in N intrinsic mode functions, $d_j(x)$, plus a residual $r(x)$ of nonzero local mean.
2. For each $d_j(x)$, estimate the amplitude function $a_j(x)$ by interpolating the local extrema.
3. Identify the positions of the zeros of $d_1(x)$ and split x in a set of successive nonoverlapping intervals (segments) between two consecutive zeros X_i for $i = 1, \dots, m - 1$; m being the total number of zeros of $d_1(x)$. (If necessary, two more intervals X_0 and X_m may be defined for the borders.)
4. For each $d_j(x)$, determine $A_{i,j} = \max_{x \in X_i} a_j(x)$.
5. For each segment X_i , define a Boolean filter $F(X_i)$ in the following way: if $A_{i,1} = \max_k A_{i,k}$, then $F(X_i) = 1$, otherwise $F(X_i) = 0$.
6. If $F(X_i)$ is identically unity, $d_1(x)$ is the sought function and the process ends. Otherwise, compute the filtered signal $s(x) = F(x)d_1(x) + \sum_{k \geq 2} d_k(x) + r(x)$ and return to step 1.
7. Normalize the envelope of the IMF and extract the phase by direct quadrature.

This algorithm is applied line by line on the profilometric images. For the EMD decomposition involved in the implementation of our algorithm, we employed the MATLAB library made publicly available in [22].

3. EMD PROFILOMETRY OF A SURFACE WITH BROADBAND SPECTRUM

In this section, we discuss the performance of the EMDP algorithm as applied to a surface characterized by a broadband height (or deformation) spectrum. Examples of such surfaces can be found in nonlinear wave interaction regimes such as wave turbulence, both in thin plates [23] and in gravity–capillary water waves [24].

We begin by considering a synthetic two-dimensional random height field $h(\vec{x}) = h(x, y)$ characterized by an isotropic power-law spectrum $S_b(k)$ given by $S_b(k) \propto k^{-\alpha}$, with α taken to be $3/2$. Numerically, such a height field is built indirectly by first defining its Fourier transform \hat{h} as

$$\hat{h}(k) = k^{-\alpha} \exp i\theta, \quad (2)$$

where i stands for the imaginary unit and θ is a two-dimensional random phase field whose values are uniformly distributed in the interval $[-\pi, \pi]$ and satisfies the condition $\theta(k_x, k_y) = -\theta(-k_x, -k_y)$, necessary for $h(x, y)$ to be real-valued. The height field $h(x, y)$ is obtained through the inverse Fourier transform of Eq. (2).

In order to simulate the profilometric process, two fringe images are created according to

$$I_r(\vec{x}) = A(\vec{x}) \cos[2\pi k_0 x] + B(\vec{x}) + N_r(\vec{x}), \quad (3a)$$

$$I_d(\vec{x}) = A(\vec{x}) \cos[2\pi k_0 x + \phi(\vec{x})] + B(\vec{x}) + N_d(\vec{x}). \quad (3b)$$

The first one constitutes a reference image in which sinusoidal fringes of spatial frequency k_0 are undeformed, whereas I_d is an image of the same fringe pattern with the apparent deformation that results from its projection onto the surface $h(x, y)$ as seen by the camera. The height information is contained in the phase $\phi(x, y)$, which is related to the height field under study via the phase-to-height relation. In turn, the functional form of this relation depends on the optical setup (parallel- or crossed-optical axes), as well as on the type of projection employed (collimated or noncollimated). For the sake of concreteness, in this section we assume parallel-optical axes and noncollimated projection. Moreover, the distance between the projector and the probed surface, usually denoted by L , is taken to be much larger than the characteristic height of the surface, so that the phase field is proportional to the height field through

$$\phi(\vec{x}) \cong -\left(\frac{2\pi k_0 D}{L}\right) h(\vec{x}), \quad (4)$$

with D being the distance between the projector's and the camera's optical axes. It is worth noting that this particular choice of optical geometry and light characteristics does not entail any loss of generality in our results concerning the performance of the EMDP algorithm.

In Eq. (3), the functions $A(\vec{x})$ and $B(\vec{x})$ represent unwanted contrast variations and background inhomogeneities, respectively. Within the framework of FTP, these functions, as well as $\phi(\vec{x})$, are required to vary slowly compared to k_0 for the method to be capable of separating their contributions.

In order to realistically simulate the profilometry process, we consider images with side length $\ell = 512$ pixels and a color depth of 12 bits. The contrast $A(\vec{x})$ is modeled by means of a paraboloidal intensity profile centered at the image center and decreasing toward its edge, mimicking the usual experimental lighting conditions

$$A(\vec{x}) = 2^{10} \left[1 - \left(\frac{r}{\ell}\right)^2 \right], \quad (5)$$

with r representing the radial distance as measured from the center of the image. In turn, the background lighting inhomogeneities are represented by

$$B(\vec{x}) = 2^{11} \left[1 - \left(\frac{r}{\ell}\right)^2 \right]. \quad (6)$$

Finally, the terms $N_r(\vec{x})$ and $N_d(\vec{x})$ in Eq. (3) correspond to (two different and uncorrelated realizations of) uniformly distributed (additive) random noise of amplitude 2^5 , representing $2^5/2^{10} \approx 3.12\%$ of the signal amplitude.

The values of the parameters associated with the optical setup are $L = 1050$ mm, $D = 150$ mm, and the fringe wavelength in the physical space $\lambda_0 = 1/k_0 = 2.5$ mm. The image physical size corresponds to a square of area (160 mm \times 160 mm), leading to a spatial resolution of $\Delta x = \Delta y = 0.31$ mm/pixels.

Figure 1(a) shows a top view of the synthetic height field $h(\vec{x})$ (built as described above) depicting the large spectral content of the original signal. For this surface, the deformed fringe pattern image $I_d(\vec{x})$ (as would be captured by a camera) is displayed in Fig. 1(b).

Based on both $I_d(\vec{x})$ and $I_r(\vec{x})$ (the latter is not shown), the proposed EMDP algorithm recovers the height field $h_{\text{EMDP}}(\vec{x})$ depicted in Fig. 1(c) for comparison purposes. In order to quantify the quality of the reconstruction locally in physical space, Fig. 1(d) shows a color map of the reconstruction error defined as $E_{\text{EMDP}}(\vec{x}) = |h(\vec{x}) - h_{\text{EMDP}}(\vec{x})|$ and is measured in mm. In this case, the mean reconstruction error gives $\langle E_{\text{EMDP}} \rangle = 0.0296$ mm, and its standard deviation is 0.0322 mm. For comparison, Fig. 1(e) shows the height field $h_{\text{FTP}}(\vec{x})$ recovered from the same reference and deformed fringe images but employing the FTP technique with a Gaussian bandpass filter centered at k_0 and typical width given by its standard deviation, set at $k_0/4 = 0.1$ mm⁻¹ (or, equivalently, a FWHM of approximately 0.24 mm⁻¹). Figure 1(f) shows the associated reconstruction error E_{FTP} . The result of the FTP analysis presents a mean reconstruction error of 0.22 mm and a standard deviation of 0.17 mm.

More importantly, we would like to determine whether our reconstructed height field presents the same power-law scaling as $h(\vec{x})$. For that purpose, we calculate the angularly averaged amplitude spectrum $S_b(k)$ and compare it to that of the imposed height field. Figure 2 presents the results of such calculation for the EMDP and the FTP reconstructed height fields, together with that corresponding to the (original) imposed height field.

As Fig. 2 shows, EMDP succeeds in reconstructing a height field which features almost exactly the same power-law dependency as the probed surface. In particular, for wavenumbers below the carrier frequency, $k \leq k_0$, the amplitude spectrum of $h_{\text{EMDP}}(k)$ is within 3% of the original $S_b(k)$. Moreover, for $k_0 < k \leq 2k_0$, the amplitude spectrum of the reconstructed surface is within 4.5% of $S_b(k)$. In this sense, EMDP overcomes the intrinsic limitation of the FTP method: the fact that the practical upper limit of the spatial resolution is 1 pitch of fringe [7].

When studying a random height field such as this, it is important that the reconstructed field not only preserves the power-law dependency of the original field but also that the data distribution be consistent with that of the original field. To address this question, we perform a two-sample Kolmogorov–Smirnov test [25] testing the null hypothesis that the recovered height field data is drawn from the same population as the original (imposed) data. For the case of the EMDP reconstructed field, the result of the Kolmogorov–Smirnov test shows that the null hypothesis cannot be rejected (with a significance level of 5%), and the associated p -value in this case is 0.980. For EMDP, failing to disprove the null hypothesis means that the original and the reconstructed fields' statistical distributions are consistent with a single distribution function. In contrast, for the FTP reconstructed height field the null hypothesis is rejected with a p -value of 5×10^{-8} , showing that the original and reconstructed height data are indeed distributed differently.

Overall, the results presented in this section show that the EMDP algorithm performs spectrally accurate reconstructions of surfaces characterized by broadband spectra of deformation. Moreover, the proposed algorithm not only outperforms FTP within its applicability domain ($k \leq k_0$) but also extends the measurable range up to $2k_0$, leading to a spatial resolution equal to half of the projected pattern wavelength ($\lambda_0/2$) in physical space.

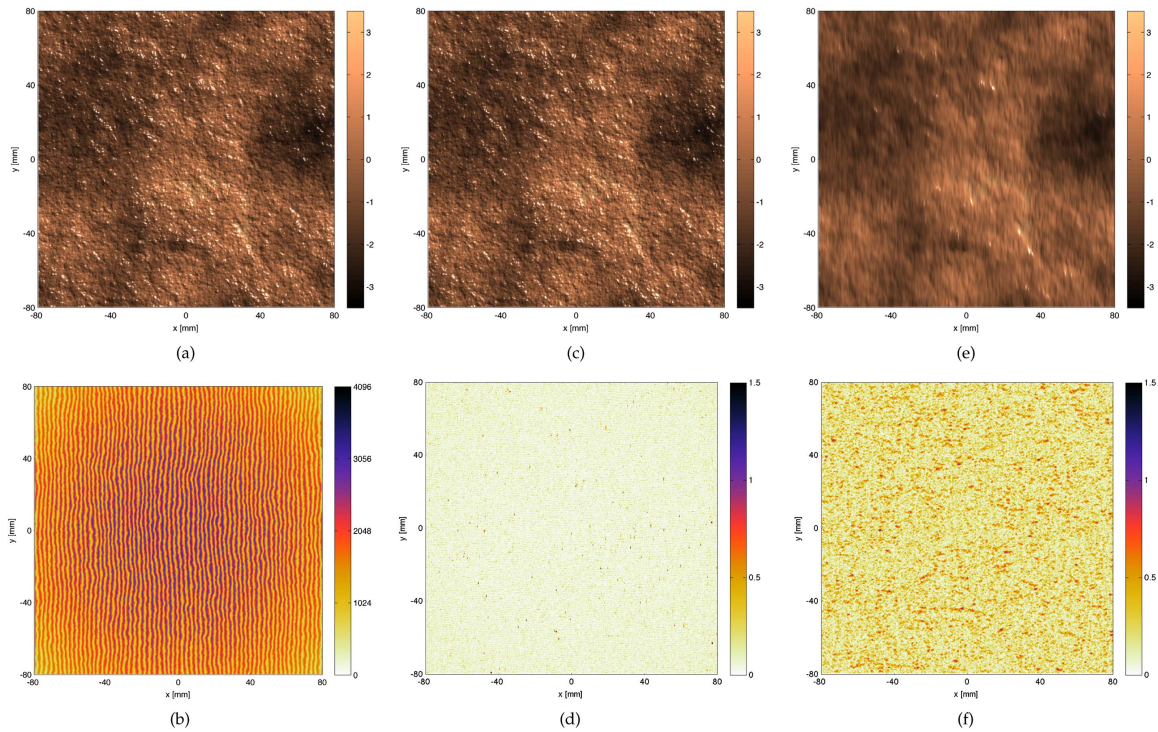


Fig. 1. (a) Synthetic two-dimensional random height field $b(\vec{x})$ characterized by an isotropic amplitude spectrum $S_b(k) \propto k^{-3/2}$. (b) Associated deformed fringe image corresponding to $I_d(\vec{x})$. (c) The recovered height field $h_{\text{EMDP}}(\vec{x})$ obtained employing the proposed EMDP algorithm. (d) The (absolute) reconstruction error for $h_{\text{EMDP}}(\vec{x})$. (e), (f) The corresponding height field recovered by FTP and its associated error, respectively. The height fields shown in panels (a), (c), and (e) have been rendered with shadow lighting in order to highlight their features. All units in mm, with the only exception of the colorbar in panel (b) which is coded between 0 and 2^{12} , corresponding to the dynamic range of the intensity image for a 12 bit camera as assumed in this study.

4. COMPARISON OF EMDP AND FTP APPLIED TO BROADBAND SPECTRUM SIGNALS

In this section we compare the performance of EMDP and FTP algorithms applied to a synthetic signal of a daisy pattern as represented in Fig. 3(a). A characteristic property of the

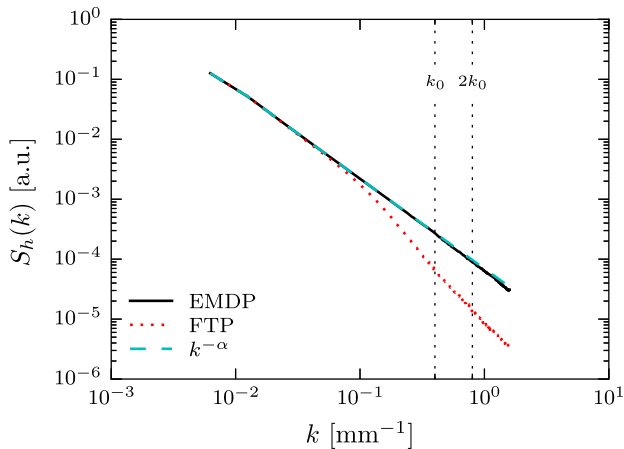


Fig. 2. Amplitude spectra of the height fields recovered by EMDP (continuous blue line) and FTP (dotted red line), as compared to that of the original (imposed) signal (dashed black line). It is observed that EMDP recovers the original spectrum slope well beyond the k_0 limit, showing that EMDP is a spectrally accurate method.

analyzed signal is that the spatial frequency increases toward the center of the imposed pattern. We generate two images, i.e., a reference fringe image with intensity variation $I_r(x, y)$ and a deformed fringe pattern $I_d(x, y)$, containing phase corresponding to the imposed surface elevation. To create synthetic fringe images, all of the parameters, i.e., fringe wavelength λ_0 , contrast variation $A(x, y)$, and lighting inhomogeneities $B(x, y)$, are chosen trying to match experimental conditions, presented in the next section. The pixel size is assumed to be 0.29 mm. The synthetic image covers an area of 232 mm \times 232 mm. The synthetic reference image is assumed to be in the form

$$I_r(x, y) = A(x, y) \cos \left[\frac{2\pi}{\lambda_0} x \right] + B(x, y), \quad (7)$$

where $\lambda_0 = 7$ mm, while $A(x, y) = -0.00275x^2 - 0.55x + 1320$ and $B(x, y) = 2A(x, y)$.

To simulate the signal in more realistic way, uniformly distributed noise is added to each of the images (amplitude of the noise is assumed to be 3%). The phase map ϕ with a daisy-shaped pattern is added to the reference signal in the form $\phi = a_1 \cos(n\theta) + a_2$, with $n = 26$, and internal radius R_1 and external radius R_2 , modulated by two Gaussian functions $f(r, \theta) = A \exp(-(r - \mu)^2/2c^2)$ at the internal and external edges. The imposed surface elevation corresponding to phase ϕ is shown in Fig. 3(a). The resulting deformed image of fringes $I_d(x, y)$ is presented in Fig. 3(b). Fringe images are analyzed

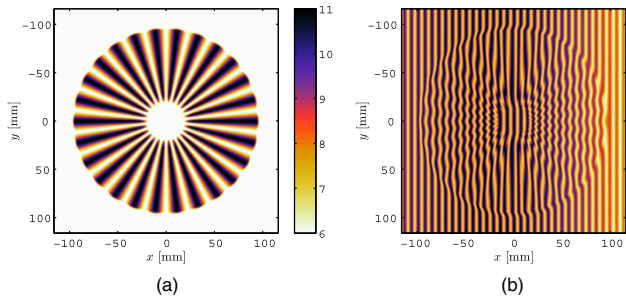


Fig. 3. Synthetic patterns: (a) imposed surface elevation corresponding to $\phi(x, y)$ and (b) fringe pattern $I_d(x, y)$ containing the imposed daisy-shaped pattern. The size of the pixel is assumed to be 0.29 mm (it is assumed that the projected pixel has the same size). Values of other parameters: $a_1 = 0.6144$, $a_2 = 2.0888$, $R_1 = 40$ pixels, and $R_2 = 350$ pixels. Gaussian function parameters: (i) internal edge $A_1 = 1, c_1 = 10, \mu = 40$ and (ii) external edge $A_2 = 1, c_2 = 10, \mu = 320$. The scale of the colorbar is in mm.

using FTP and EMDP algorithms. Reconstructed surface elevation fields using both methods are presented in Figs. 4(a) and 4(b). Figures 4(c) and 4(d) show the logarithm of absolute errors of the surface elevation in each case. To quantify the accuracy of FTP and EMDP standard deviation of error maps as a function of radius are determined (see Fig. 5). Different Gaussian filter sizes, i.e., Gaussian RMS width σ , are taken into account for FTP reconstruction. As the filter size increases, the accuracy of amplitude determination increases. However, for a filter size of $\sigma \geq 0.36k_0$ artifacts appear, which are visible in Fig. 5, in the form of undesirable oscillations. The origin of these oscillations is strictly associated with the sampling of fringe pattern [6]. For any filter size applied to FTP, one can notice superiority in EMDP reconstruction. EMDP copes well with rapid changes of slopes in the imposed surface elevation,

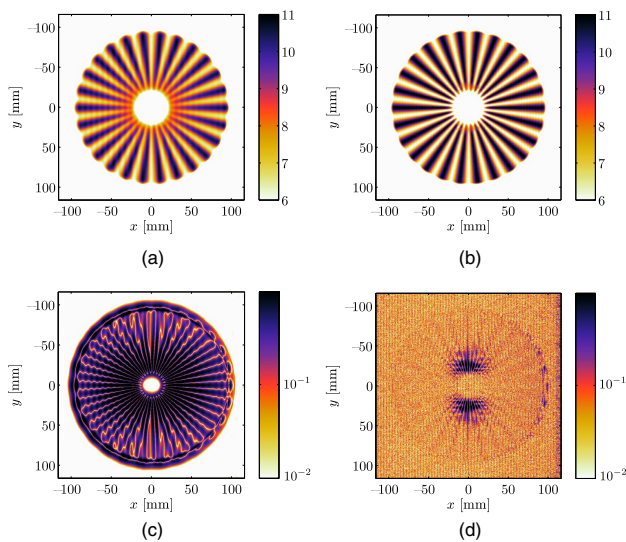


Fig. 4. Comparison of EMDP and FTP applied to a synthetic daisy-shaped field: (a) FTP results with a filter size of $\sigma = 0.36k_0$, (b) EMDP results, (c) absolute error of FTP reconstruction, and (d) absolute error of EMDP reconstruction.

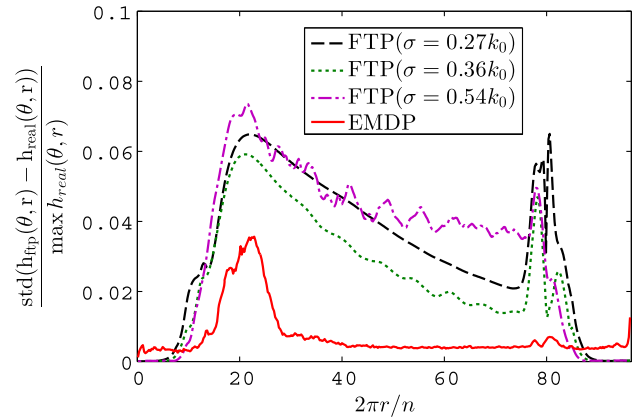


Fig. 5. Accuracy of EMDP and FTP. FTP results are presented for different filter size σ .

for example, at the external edge, whereas error obtained with FTP drastically increases wherever such changes are present in the signal.

5. EXPERIMENTAL VALIDATION

In this section we present experimental validation of the numerical results concerning a daisy-shaped pattern. The model, designed with a surface elevation corresponding to the synthetic phase ϕ , is manufactured using the rapid prototyping technique. The accuracy of the model is 0.1 mm in all (x, y, z) directions and is due to limitations of the printer. The obtained physical model is presented in Fig. 6. The fringe pattern is projected using a high-resolution projector (1920 pixels \times 1080 pixels). Images are captured using a Phantom SA4 camera with a resolution of 1024 pixels \times 800 pixels. The entrance pupils of the projector and camera are set at the same distance $L = 1050$ mm from the reference plane, while the horizontal distance between them is $D = 250$ mm. The size of the projected pixel is around 0.39 mm, while $\lambda_0 = 7$ mm.

The reconstructed surface elevation fields, using both methods, are shown in Fig. 7. Significant influence of the shadows can be observed in the center of the model. Nevertheless, the obtained experimental surface elevation fields confirm superiority of EMDP as it can resolve higher spatial frequencies in



Fig. 6. Photograph of the experimental model produced with the rapid prototyping technique. In the right top of the figure, a 2-euro coin is shown for size comparison.

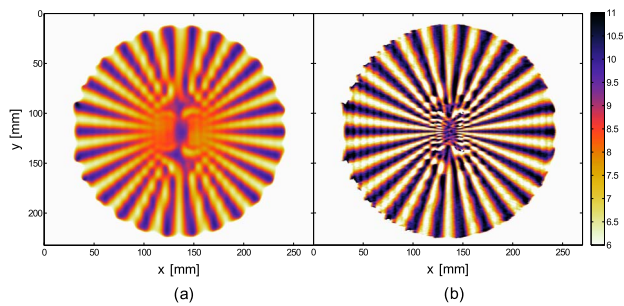


Fig. 7. Experimental results: (a) FTP with $\sigma = 0.29k_0$ and (b) EMDP. The scale of the colorbar is in mm.

the center of a daisy pattern with better accuracy in amplitude determination.

6. CONCLUSIONS

We have presented a comparison of the performance of the usual FTP and the EMDP. In the past years, the need for performing accurate noncontact measurements has motivated studies on signal processing to enhance the quality of the height reconstruction in these methods. The EMD is based on an iterative filter which avoids any spatial filtering. This results in enhanced capabilities of the method for the small scales. Numerical and experimental examples of these capabilities have been provided together with a comparison with the Fourier transform technique as used in standard FTP.

Funding. Agence Nationale de la Recherche (L'Agence Nationale de la Recherche) (DYNAMONDE ANR-12-BS09-0027-01); Consejo Nacional de Investigaciones Científicas y Técnicas (National Scientific and Technical Research Council) (Carrera del Investigador Científico); Universidad de Buenos Aires (University of Buenos Aires) (UBACYT 20020110200359).

Acknowledgment. The authors wish to thank P. Flandrin and P. Borgnat for fruitful discussions.

REFERENCES

- S. Zhang, *Handbook of 3D Machine Vision: Optical Metrology and Imaging*, Series in Optics and Optoelectronics (Taylor & Francis, 2013).
- P. J. Cobelli, A. Maurel, V. Pagneux, and P. Petitjeans, "Global measurement of water waves by Fourier transform profilometry," *Exp. Fluids* **46**, 1037–1047 (2009).
- A. Maurel, P. Cobelli, V. Pagneux, and P. Petitjeans, "Experimental and theoretical inspection of the phase-to-height relation in Fourier transform profilometry," *Appl. Opt.* **48**, 380–392 (2009).
- M. Takeda, H. Ina, and S. Kobayashi, "Fourier-transform method of fringe-pattern analysis for computer-based topography and interferometry," *J. Opt. Soc. Am.* **72**, 156–160 (1982).
- M. Takeda and K. Mutoh, "Fourier transform profilometry for the automatic measurement of 3-D object shapes," *Appl. Opt.* **22**, 3977–3982 (1983).
- W. Chen, H. Yang, X. Su, and S. Tan, "Error caused by sampling in Fourier transform profilometry," *Opt. Eng.* **38**, 1029–1034 (1999).
- B. Zhao and A. Asundi, "Discussion on spatial resolution and sensitivity of Fourier transform fringe detection," *Opt. Eng.* **39**, 2715–2719 (2000).
- S. S. Gorthi and P. Rastogi, "Fringe projection techniques: whither we are?" *Opt. Lasers Eng.* **48**, 133–140 (2010).
- X. Su and W. Chen, "Fourier transform profilometry: a review," *Opt. Lasers Eng.* **35**, 263–284 (2001).
- N. E. Huang, Z. Shen, S. R. Long, M. C. Wu, H. H. Shih, Q. Zheng, N.-C. Yen, C. C. Tung, and H. H. Liu, "The empirical mode decomposition and the Hilbert spectrum for nonlinear and non-stationary time series analysis," *Proc. R. Soc. Lond. A* **454**, 903–995 (1998).
- Z. Wu and N. E. Huang, "Ensemble empirical mode decomposition: a noise-assisted data analysis method," *Adv. Adapt. Data Anal.* **01**, 1–41 (2009).
- P. Flandrin, G. Rilling, and P. Gonçalves, "Empirical mode decomposition as a filter bank," *IEEE Signal Process. Lett.* **11**, 112–114 (2004).
- P. Flandrin, P. Gonçalves, and G. Rilling, "Detrending and denoising with empirical mode decompositions," in *12th European Signal Processing Conference* (IEEE, 2004), pp. 1581–1584.
- S. Li, X. Su, W. Chen, and L. Xiang, "Eliminating the zero spectrum in Fourier transform profilometry using empirical mode decomposition," *J. Opt. Soc. Am. A* **26**, 1195–1201 (2009).
- X. Zhou, H. Zhao, and T. Jiang, "Adaptive analysis of optical fringe patterns using ensemble empirical mode decomposition algorithm," *Opt. Lett.* **34**, 2033–2035 (2009).
- C. Wang and F. Da, "Phase demodulation using adaptive windowed Fourier transform based on Hilbert–Huang transform," *Opt. Express* **20**, 18459–18477 (2012).
- S. Zheng and Y. Cao, "Fringe-projection profilometry based on two-dimensional empirical mode decomposition," *Appl. Opt.* **52**, 7648–7653 (2013).
- C. Wang and F. Da, "Differential signal-assisted method for adaptive analysis of fringe pattern," *Appl. Opt.* **53**, 6222–6229 (2014).
- N. E. Huang, Z. Shen, and S. R. Long, "A new view of nonlinear water waves: the Hilbert spectrum," *Annu. Rev. Fluid Mech.* **31**, 417–457 (1999).
- N. E. Huang and Z. Wu, "A review on Hilbert–Huang transform: method and its applications to geophysical studies," *Rev. Geophys.* **46**, RG2006 (2008).
- N. E. Huang, Z. Wu, S. R. Long, K. C. Arnold, X. Chen, and K. Blank, "On instantaneous frequency," *Adv. Adapt. Data Anal.* **1**, 177–229 (2009).
- G. Rilling, P. Flandrin, and P. Gonçalves, "On empirical mode decomposition and its algorithms," in *Proceedings of the 6th IEEE/EURASIP Workshop on Nonlinear Signal and Image Processing*, Grado, Italy, 2003.
- P. Cobelli, P. Petitjeans, A. Maurel, V. Pagneux, and N. Mordant, "Space-time resolved wave turbulence in a vibrating plate," *Phys. Rev. Lett.* **103**, 204301 (2009).
- P. Cobelli, A. Przadka, P. Petitjeans, G. Lagubeau, V. Pagneux, and A. Maurel, "Different regimes for water wave turbulence," *Phys. Rev. Lett.* **107**, 214503 (2011).
- M. DeGroot and M. Schervish, *Probability and Statistics* (Addison-Wesley, 2012).